

Numerical Tracing of Energetic Particle Drifts in a Model Magnetosphere

G. D. REEVES, R. D. BELIAN, AND T. A. FRITZ

Los Alamos National Laboratory, Los Alamos, New Mexico

We present results from a model developed to study the motion of impulsively injected energetic particles which become trapped in the Earth's magnetic field at geosynchronous orbit. The model is based on numerically solving the analytic expressions for the bounce average gradient and curvature drift in a model magnetic field. The predicted motion of trapped geosynchronous particles in the Tsyganenko and Usmanov (1982) model (TU-82) has characteristics which are not predicted by less sophisticated models. We investigate the motion of drifting particles predicted by the model under various conditions such as: Kp level, pitch angle, orientation of the magnetic field, and location of the origin of the drift shell. As a test of the predictions of the model, we apply it to observations of a substorm injection event which took place on October 16, 1983, and was observed by three geosynchronous satellites. The injection region for this event is found to span approximately 45° from near midnight to near 2100MLT. We also report the existence of a "periphery" outside the central injection where either injected ions or electrons, but not both, are observed with dispersionless signatures. The internal consistency of the predictions of the structure of the injection region using remote observations from the three geostationary satellites and the TU-82 field model is found to be quite good.

INTRODUCTION

The physical principles which govern the motion of charged particles in the Earth's magnetic field are well understood [e.g., *Roederer*, 1970]. However, the actual motion of particles in the magnetosphere is less well understood, largely due to the fact that the large scale geomagnetic field is not well known. Thus the large-scale structure of the Earth's magnetic field must be obtained from a model. In this paper we analyze the motion of charged particles in the semi-empirical model magnetic field of *Tsyganenko and Usmanov* [1982] (hereinafter referred to as TU-82).

For many applications, drift motion in a dipole field does not adequately approximate drift motion in the real field, making it impossible to consistently interpret observations of trapped geosynchronous particles. In the real geomagnetic field, compression of the dayside and stretching of the nightside fields produce appreciable effects on particle drift motion. The TU-82 model includes magnetopause and tail current systems so we can model the magnitude of these effects. In a dipole field, analytic expressions for the bounce-averaged gradient and curvature drift velocity can be written in closed form [e.g., *Roederer*, 1970]. In a more complicated field geometry they must be solved numerically. Using a model field, we can trace field lines to determine how distortions of the field, such as increased stretching of the tail, affect the bounce average drift motion. We can compare bounce-averaged drift motion to purely equatorial drifts to determine the validity of that simplifying assumption. We can also investigate the shape of

drift shells under various field configurations and model drift shell splitting for particles with different pitch angles. The results have important consequences for the interpretation of geosynchronous energetic particle data.

Geosynchronous altitudes are interesting for several reasons. (1) The magnetic field contains measurable contributions from the major magnetospheric current systems but is less dynamic than, say, the magnetotail. (2) Simultaneous measurements of energetic particles from satellites at several local times are available, and these satellites often measure the same population of drifting particles. (3) During substorms, populations of energetic particles, which can be distinguished from the preexisting population, are deposited on near-geosynchronous drift shells.

Injections of energetic particles at geosynchronous orbit are well suited for studying the drift motion of trapped particles and comparing that motion with the predictions of models. Many injections are impulsive and occur in a limited range of local times. Injections often accompany the release of stored magnetic energy in the tail [*Belian et al.*, 1981] so, following injections, the geosynchronous field is often relaxed and varying slowly in time. Simultaneous measurements from geosynchronous spacecraft allow one to follow the motion of injected particles. As observed within a limited band of energies the injected particles appear as a pulse. Measurements of injected particles in several energy bands show dispersion due to differential drift velocities. As *Akasofu* [1977] points out, "the crucial problem is how to interpret, without contradiction, the apparent

dispersion effect of the entire range of observed energies of both protons and electrons." We will show that, with an adequate understanding of particle motion in the TU-82 field model, a consistent interpretation is possible.

The energetic particle data used in this paper were obtained with the Los Alamos charged particle analyzer (CPA) instrument which has flown on a series of geosynchronous satellites since 1976. Typically, three satellites are in operation at any given time. The CPA measures protons in the equatorial plane of each spacecraft every 256 ms with 10 integral energy channels between ≈ 100 and ≈ 600 keV and 16 differential energy channels from ≈ 0.4 to ≈ 150 MeV. Energetic electrons are also measured in the spacecraft equatorial plane with six integral channels in the energy range ≈ 0.2 to ≈ 1.5 MeV. Electrons in the energy range ≈ 30 to ≈ 300 keV are measured in six energy channels at angles of 0° , $\pm 30^\circ$, and $\pm 60^\circ$ from the spacecraft spin plane. The spin axis of each spacecraft points radially toward the Earth, and the spin period is 10 s. In general (and throughout this paper), spin-averaged data are used. This, in turn, implies that all data include contributions from a broad range of pitch angles. None of these spacecraft is equipped with a magnetometer. More complete descriptions of the CPA instruments can be found in works by *Higbie et al.* [1978], *Belian et al.* [1978], and *Baker et al.* [1979, 1985].

The relationship between energetic particle enhancements observed at geosynchronous orbit and magnetospheric substorm activity measured by ground-based magnetometers and satellites in the magnetotail has been discussed by *Baker et al.* [1979], *Belian et al.* [1981], and references therein. Studies of energy dispersion and drift of injected particles have been reported by *Pfitzer and Winckler* [1969], *Brewer et al.* [1969], *Arnoldy and Chan* [1969], *Bogott and Mozer* [1973, 1974], *Kivelson and Southwood* [1975], *DeForest and McIlwain* [1971], *Chanteur et al.* [1977], *Walker et al.* [1978], *Belian et al.* [1978], and *Reeves et al.* [1990]. A major conclusion of these studies is summed up by *Walker et al.* [1978 p.1595] who state that "At local times after dusk the observations (of ion drifts) support a simple model of acceleration and drift in a dipolelike field, but in the afternoon and morning sectors this simple model does not even qualitatively explain the observations."

Our results are divided into three sections. In the first section we discuss the magnetic field model itself and the implementation of the theories of guiding-center drift in a model magnetic field. Next we consider some of the basic characteristics of particle drifts in the model field by analyzing the dependence of drift motion on various parameters. In the third section we discuss the application of the

drift model to observations of energetic particle injections.

HOW THE DRIFT MODEL WORKS

The Field Model

The *Tsyganenko and Usmanov* [1982] magnetospheric field model provides a magnetic field vector at any point in the magnetosphere given the position, date, and time. The date and time are used to obtain the appropriate terrestrial magnetic field from the International Geophysical Reference Field (IGRF 1982) model. Superimposed on the terrestrial field are the contributions from the magnetospheric ring current, the magnetotail current sheet, and the magnetopause current. The effect of these three current systems on the total magnetospheric field are obtained from mathematical descriptions. The ring and tail currents are modeled explicitly. The magnetopause current and the average effect of all other currents are treated by a power series expansion [*Mead and Fairfield*, 1975] with an additional exponential dependence on the x -coordinate. The formulae for these magnetic field contributions contain 21 linear and 7 nonlinear adjustable parameters. The values of these parameters are obtained through an optimization routine which fits the model fields to sets of IMP-HEOS magnetic field data. The data are binned according to 11 ranges of Kp from 0 to $>3^+$, and one set of parameters is derived for each range of Kp [*Tsyganenko and Usmanov*, 1982].

Figures 1-3 illustrate some of the characteristics of the TU-82 field around geosynchronous orbit. Figure 1 shows the shape of field lines at local noon, midnight, and dusk for conditions of a stretched field ($Kp=3$). Throughout this paper we often consider the time June 21, 16.67 UT because at this time the Earth's rotational and magnetic dipole axes lie nearly in the GSE x - z plane and point toward the Sun. Hence there is a clear sunward/antisunward asymmetry but little dawn/dusk asymmetry. The field lines shown in Figure 1 were traced from the geographic equator at $6.6 R_E$ and then rotated into a coordinate system defined by the line from the Earth's center to the magnetic equator. We see that the field lines at noon and at dusk are fairly symmetric about the magnetic equator while the field line at midnight is distorted by the stretch of the tail and the tilt of the dipole. A comparison of the field lines at noon and dusk shows the compression of the field at noon. Since the TU-82 model is binned according to Kp alone, high Kp levels imply both compression of the nose and stretching of the tail fields. The two conditions are not treated independently. This has implications for substorm injections in which the tail may become

more dipolelike because of release of magnetic energy, while the nose remains compressed.

Figure 2 shows a comparison of measured and model field magnitudes. The magnetic field data was obtained by the geosynchronous GOES 2 spacecraft on August 12, 1988, and is plotted with a bold line. The model field magnitudes were calculated for the appropriate orientation of the terrestrial field, at the location of GOES 2, for two disturbance levels: $Kp=0$ and $Kp>3^+$. We see that the model agrees with the data reasonably well but has obvious shortcomings. The rapid fluctuations of the field are not reproduced. Comparison of the beginning and the end of the measured field trace show a longer-term variation of the field which is also not reproduced by the model. At the end of the trace there is good agreement, while at the beginning of the trace, 24 hours earlier, we find relatively poor agreement. We hasten to point out that the difference between the model and the measured field is likely to be greater near the equator than the average difference between fields sampled by charged particles in their bounce motion along the field.

Figure 3 illustrates why this is so. In this figure, three model field lines at local midnight are shown. The "original field line" is traced from a hypothetical satellite at $6.6 R_E$ on the geographic equator for relaxed conditions of $Kp=0$. A field line traced from the same location for stressed conditions of $Kp=3$ has nearly the same shape. The third field line is traced from the point where the "original field line" ($Kp=0$) intersects the Earth's surface, and this field line again has $Kp=3$. We see that although the shape of the field line through the geographic equator changes little, the magnitude at the equator can change substantially. At higher latitudes though the field magnitude will change less dramatically. All the above characteristics of the TU-82 model magnetic field should be kept in mind when we calculate the bounce and drift motion of charged particles.

The Drift Model

The drift model solves the analytic equations for the guiding centers of the particles [e.g., Roederer, 1970]. Since the expression for the magnetic field is too complicated to be treated analytically, the equations are solved numerically. Figure 4 is a schematic of the method we use. The starting point for the calculation is generally the location of a spacecraft which observes a particle signature we wish to trace (for example, a substorm injection pulse). The magnetic field line is traced using a fourth-order Runge-Kutta differential equation solving technique [Fehlberg, 1970]. Since we will be integrating quantities along the magnetic field, it

is very important to trace the field to high accuracy. We trace the field using an adaptive step size which tests that the maximum of error in position along the field, the error in the field magnitude, and the error in the integrands of interest are less than a specified value. Contrary to what is implied in Figure 2, the number of steps which define a field line typically exceeds 10,000.

For a given pitch angle the mirror points (m_1 , m_2) and the magnetic equator are determined. Next the invariant integral,

$$I = \int_{m_1}^{m_2} \frac{B(s)}{B_m} ds,$$

is calculated using a simple trapezoid integration. (Here s is along the field line and B_m is the mirror field magnitude.)

The drift shell is defined by an arbitrary number of field lines (N) which share the same values of the first and second adiabatic invariants. As illustrated in Figure 2, once the mirror points and the invariant integral are calculated for the original field line the code looks for a new field line at a new longitude $\Delta\lambda$ away. The latitude, longitude, and mirror field magnitudes are kept fixed while the radius is varied. Field lines are traced at various radii, and an inverse quadratic interpolation method [Brent, 1973] is used to narrow in on the one for which I is conserved to within specified precision. Typically, we use 36 to 100 field lines which are equally spaced in longitude to define the drift shell and require that I be constant to within 0.1%.

Once the model drift shell has been determined the next step is to calculate the bounce averaged drift velocity for each of the N field lines which define the shell. The bounce average drift velocity is given by

$$V_D = \langle V_{GC} \rangle = \frac{2E}{qS_b B_0} \frac{\partial I}{\partial \lambda} \frac{\hat{B}_0}{B_0}$$

where V_{GC} is the gradient-curvature drift velocity, E is the kinetic energy, the subscript 0 denotes values at the equator and

$$S_b = \int_{m_1}^{m_2} \frac{B(s)}{B_m} ds,$$

is the so-called half-bounce path length. Calculation of the gradient of I is time consuming but uses a straightforward Stirling approximation [Dahlquist and Björck, 1974]. The quantity S_b is sensitive to errors in the integration especially near the mirror points where there is an integrable singularity. Therefore, in addition to using the error in the integrand of S_b to set the step size along the field line, we also use spline interpolation and adaptive quadrature to perform the integration [Forsythe et al., 1977].

As a final step the bounce average drift velocity is converted to angular velocity and the time required to drift through the angle $\Delta\phi$ from one field line to another is calculated. These times Δt can be summed to determine the time required to drift through a given angle or to determine the total drift period.

DRIFT MOTION IN THE TU-82 MODEL FIELD

The bounce average drift velocity can be quite different from the gradient and curvature drift velocities at a given point. This is particularly important when the particles measured are not 90° pitch angle particles as is often assumed. Figure 3 shows gradient and curvature velocities along various field lines. In Figure 3a we have traced a field line for a 45° , 100-keV proton at noon starting from $6.6 R_e$ along the geographic equator. The dashed and dotted curves are the gradient and curvature drift velocities respectively for $Kp=0$. The bold curve is the sum of the gradient and curvature drifts for $Kp=0$. The solid (not bold) curve is the sum of gradient and curvature drifts for $Kp=3$. The curves for $Kp=0$ show the classic shapes one expects for a nearly dipole field with the exception of a slight north/south asymmetry due to the dipole tilt. For $Kp=3$, however, the effects of compression of the field are apparent, particularly, the relative lack of curvature near the equator which reduces the curvature drift velocity. An important consequence is that at noon, when the field is compressed, 90° pitch angle particles may drift more slowly than, say, 60° particles which experience larger gradient-curvature drifts at higher magnetic latitudes on the same field line.

Figure 3b again compares the gradient-curvature drift velocities along field lines. Curves are plotted for field lines at noon, dusk, and midnight. The curve for noon is the same as that plotted in Figure 3a for $Kp=3$. The other two curves are for field lines on the same drift shell. In other words, all three field lines have the same first two adiabatic invariants. The bounce average drift velocities for each field line are also indicated in the bottom of the figure. For field lines at noon there is little difference between the bounce average drift velocity and the drift velocity near the equator. For field lines at midnight the difference is more than a factor of 2. We can also see that the difference in drift velocities at a given magnetic latitude, as the particles drift around the shell, can be quite large while variations in the bounce average drift velocity are less dramatic.

The bounce average drift velocities at various local times are shown in Figure 4. Curves for three disturbance levels are plotted. Again, the drift shell is defined for a hypothetical 100-keV, 45° proton

starting at $6.6 R_e$ on the geographic equator at noon. For $Kp=0$ we see the expected behavior. Drift velocities are slowest on dayside and fastest on the nightside. For higher disturbance levels, however, an interesting behavior emerges. Drift velocities at midnight are somewhat slower than they are on either side. This reflects a local increase in the half-bounce path length S_b near midnight. This is related to the shape of the field line shown in Figure 1. Field lines near midnight are shaped more like those at dusk but the gradients and curvatures are larger. This feature appears to be related to the form of the tail current in the TU-82 model. One should also note that in a dipole field the drift velocity is constant around the drift shell while in the TU-82 field this is not even approximately true.

It is also interesting to look at the shape of the model drift shells for various Kp values. In Figure 5 we show the radial distance to the magnetic equator as a function of local time for the same three drift shells as discussed above. The difference in equatorial radii at noon is due to the fact that the starting point is $6.6 R_e$ radial distance, at the geographic equator which is at somewhat different magnetic latitudes for different Kp values. We see a noon/midnight asymmetry which is larger for higher Kp values. However, this stretching is less than $0.4 R_e$, and the difference between $Kp=0$ and $Kp=3$ is about $0.1 R_e$. When these curves are plotted in a polar format the drift shells appear circular and nearly overlap. This bears note because the amount of stretching of the drift shell has important consequences for the interpretation of substorm dynamics. Two effects are at play here. First, the TU-82 field model most likely does not provide enough distortion in the tail to correctly represent the real stressed field. This is to be expected from a model which fits average conditions. Second, the effects of the bounce motion of the 45° pitch angle particles will mitigate the effects of stretching of the tail by bounce averaging over higher latitude, less distorted field lines.

Figure 6 shows pitch angle splitting of drift shells in the same format as Figure 5. Once more, curves are for a 100-keV proton starting at noon with $Kp=3$. Four pitch angles, 5° , 30° , 60° , and 85° , are shown. The pitch angles are defined at the starting point which, in this case, is the geographic equator. For these conditions the maximum splitting at midnight compared to drift at a constant radial distance is about $0.6 R_e$. Figure 6 can be compared to Figure 48 of Roederer [1970] which shows, qualitatively, the same behavior for calculations in the Mead-Fairfield model.

When we look at drift velocities along these same shells, however, there are some surprises. Figure 9 shows angular drift velocity as a function

of time along the drift shells plotted in Figure 8. At midnight higher pitch angles have higher drift speeds as we would expect. We can see that, at noon, this is not the case. In fact, 85° ions drift more slowly than 5° ions and both drift more slowly than 30° or 60° ions. This is a consequence of the compression of the field as we have already seen in Figure 4. The combination of drift shell splitting and the compression of the field at noon is that the drift period for 85° , 100-keV protons which start at noon is actually longer than the drift period for those with 60° pitch angles. The point is that conventional wisdom about the drift motion of charged particles may not accurately reflect their behavior in a realistic magnetic field.

Up to this point, we have considered quantities on drift shells defined by a starting point at local noon and by a geometry in which the dipole axis, the rotation axis, and the Earth-Sun axis are nearly coplanar. Figure 10 shows the invariant integral and the magnetic field magnitude at hypothetical satellite locations at $6.6 R_E$ in the geographic plane at various local times. For each point the time is fixed at June 21, 1983, 16.67 UT so the field geometry is unchanging. The variation in the magnitude of the field contains both noon/midnight asymmetries and the effect of changes in the magnetic latitude of the geographic equator. The pitch angle is defined at the geographic equator as 45° for each local time. Thus the change in magnetic equatorial pitch angle as well as the shape of the field line is included in the variation of the invariant integral.

Figure 11 shows a similar effect but under different circumstances. In this case we have allowed the time to vary through 24 hours, while keeping the location of the satellite fixed at local noon. In effect, we sit at a fixed location in space, while the Earth and the terrestrial field rotates. The abscissa in the plot is the direction the magnetic dipole points with respect to local noon. It is clear from these two figures that the orientation of the geographic and geomagnetic coordinate systems can determine which adiabatic invariants are appropriate for a given set of observations.

APPLICATION OF THE DRIFT MODEL

In this section we apply the results of the drift model described above to an energetic particle injection observed on October 16, 1983 at approximately 4.9 UT. Three geosynchronous spacecraft carrying CPA instruments were in operation at the time. For simplicity, we will refer to them as spacecraft A, B, and C. They were located at -133.6° , -70.0° , and 69.7° geographic longitude respectively. This put spacecraft A near 2000 UT, spacecraft B near local midnight, and spacecraft C

just prior to local noon. The latitudes were -0.2° , 0.3° , and 4.7° .

Figure 12 shows the location of the three spacecraft at the time of injection. The drift shell defined by 45° particles and the location of each spacecraft is also shown. Positions in the X-Y GSE plane are plotted by projecting the magnetic equator of each field line into the ecliptic plane. We see that spacecraft B and C share nearly the same drift shell, while spacecraft A lies on a drift shell approximately $1/4 R_E$ further away. The injection region is also sketched in the figure. This was a particularly fortuitous configuration of spacecraft locations for this particular event in that the injection region could be inferred directly from observations at spacecraft A and B. Our analysis assumes that the injection has the same properties on the drift shells connected to both spacecraft A and B.

Figure 13 shows electron and ion signatures of the injection for spacecraft A and B. Flux is plotted in arbitrary units with curves for each energy band offset so that their shapes are more readily discernable. The electron signatures seen on spacecraft B show the following "classic" features observed near midnight [Belian et al., 1981]. About 1 hour prior to the injection, fluxes drop dramatically which is often taken as evidence of the substorm growth phase. Fluxes then rise very rapidly, beginning at 4.86 UT, up to levels an order of magnitude higher than ambient levels. Since the impulsive injection of electrons observed on spacecraft B is dispersionless, we conclude that electrons were observed before they had time to drift any appreciable distance. There is then a fairly rapid decline in flux levels signifying the end of the injection. At later times, drift echoes [Brewer et al., 1969] are observed with energy dispersion consistent with drift through almost 360° as we will show below.

The ions observed at spacecraft B show a more complicated response. The growth phase decrease in flux levels and the dispersionless onset of the injection coincide with what is seen in the electron fluxes. In the two lowest-energy channels (for example, the upper curve in the plot) some transient flux increases are observed immediately following the injection onset. At higher energies an increase in flux levels immediately following the onset is not observed (for example, the lower curve in the plot). Rather, flux levels return, for a short time, to pre-event levels before the injection pulse is observed. A full set of energy bands (not shown) would show that these delayed pulses have energy dispersion which is consistent with drift through about 320° .

The ion and electron fluxes for spacecraft A show similar behavior but with the roles of electrons and

ions reversed. The ion signatures show the “classic” response with the exception that the decline in fluxes prior to injection is much less dramatic than at midnight. The onset of the ion injection is dispersionless and, immediately following onset, fluxes rise to levels about an order of magnitude higher than before the event. At later times, ion drift echoes appear. For the electrons, onset is followed by a relatively slow increase which levels out at fluxes somewhat lower than pre-event values. When the injection pulses are observed some time later, they are dispersed in energy.

Under typical conditions a geosynchronous spacecraft near midnight will simultaneously observe dispersionless injection of both ions and electrons. We interpret the signatures of Figure 13 as evidence that spacecraft A and B lie in a region which we call the injection periphery. Close scrutiny of the peaks of the injection pulses seen in the electrons at spacecraft B and the ions at spacecraft A reveal a small amount of energy dispersion while, as mentioned, the onset of injection is dispersionless. This suggests that the two spacecraft lie near the edges of the injection region. The fact that spacecraft A observes the ion peaks immediately following onset but observes the electron peaks only after they have drifted nearly around the Earth suggests that the ion injection region extends further west than the electron injection region. Electron and ion signatures at spacecraft B show the opposite behavior indicating that the electron injection region extends further east. We can therefore define the ‘central’ injection region as that span of local time in which electrons and ions are injected together. The ion ‘injection periphery’ is then the region to the west of the central injection where ions but not electrons are injected and the electron periphery is the region to the east where electrons are injected but ions are not.

The fortuitous occurrence of the substorm injection between spacecraft A and B provides us with an excellent opportunity to test our drift shell model. There is a third satellite near local noon which observes both electron and ion injection pulses drifting from the injection region. We have taken those remote observations and projected them back along the drift shell to see how well they agree with what is directly measured.

We know the time of injection from direct observation so we initialize the field for this time to get the proper field geometry. We also know the locations of the three spacecraft. What we do not know is what Kp value to use in the TU-82 model or what pitch angles to use in the drift model. At the time of injection Kp was 4-. What we need to know, however, is not how active the magnetosphere was around this time but how distorted was the field

immediately after the injection since that is what affects the particles drift. We can evaluate the TU-82 by comparing measured and model drift periods. Fortunately, the electron signatures from spacecraft B show clear drift echoes in seven energy bands. The drift echoes tell us the drift period which can be compared to the model to constrain Kp and the pitch angle (α). This comparison is shown in Figure 14. The solid line represents what would be full agreement between model and measured drift periods. The points show the correlation between model and measured drift periods up to almost 4 hours. A least squares fit is plotted with long dashes for $Kp=0$ and with short dashes for $Kp=3$. The differences between the model predictions for the two Kp levels are not large compared to the measurement errors, but we find in general that $Kp=0$ gives a better agreement for isolated substorms. The likely explanation is that, since injections accompany relaxations of the field, immediately following an injection the field looks like a quiet time field with $Kp=0$. The choice of 45° for the pitch angle is somewhat arbitrary. Pitch angles of 45° generally give good results for the peak of the injection pulse. From Figure 14 we can see 90° pitch angles (which would give smaller model drift periods) would give worse agreement, while smaller pitch angles would give slightly better agreement. Nevertheless, we decided to use a 45° pitch angle as a nominal pitch angle for our calculations since, for most applications, one does not have measured electron drift periods available to optimize the fit.

To project the observations from spacecraft C back along the drift shell we plot the drift motion of ions or electrons in local time and universal time. Figure 15 shows such a plot for ions. One line is plotted for each of nine energies from 117 keV to 450 keV. The slope of each line is related to the drift velocity, steeper slopes indicating slower drifts. The time and location at which the peak of the ion pulses were observed for each energy is plotted in the upper left, and the dispersion in arrival times is reflected in the different starting points for each line. Using drift velocities computed by the model, we project back along the drift shell in steps of 1° and 1° through 360° . If all energies were injected together at the same time and location, the projections should intersect at a single point. Because of uncertainties in the arrival times of the injection peaks (particularly the 300-keV channel), the lines instead converge to a broader area. We take the center of this convergence area as the injection location.

Figure 16 shows the spatial extent of the injection region determined by direct measurement and by various projections. Spacecraft A was located at -60.8° from local midnight and saw a

dispersionless injection of ions but not electrons. The ion injection peaks observed on spacecraft A were projected in the same way as peaks observed on spacecraft C. They project to an injection location at -48° . Spacecraft B made direct measurements of the electron periphery at $+2.8^\circ$ from local midnight and the electron peak projects to -2° . The projections of ions and electrons from spacecraft A and B are very reliable. The observed arrival times of the peaks are well defined, and the projection is over a very short distance and hence depends weakly on the assumed model field. The central injection region is therefore defined as extending from -48° to -2° as is shown in the figure. The projections of electron and ion peaks observed on spacecraft C predict that the injection region lies between -47° and -4° , in excellent agreement with the local measurements from the other two spacecraft.

The projections of observations back to the injection region also provide a means to remotely measure the injection time. Spacecraft A measured ions injected starting at 4.86 hours UT and spacecraft C measured electrons injected at 4.88 UT. The projections from spacecraft C predict that ions were injected at 4.87 UT and electrons at 4.90 UT. The ion injection peaks observed at spacecraft B were not directly injected but rather had drifted west around the Earth. The ion injection time predicted from those peaks is 4.88 UT. The electron injection time predicted from electrons which drifted east to be observed at spacecraft A is 5.06 UT. These times are all in agreement to within about 1 min. We also note that, to within this accuracy, electrons, and ions were injected simultaneously.

It should be noted that the electron projections are presented with the following caveat. The electrons used in the analysis had energies in the range 30-140 keV. Therefore relativistic effects may be important. Our drift model code and therefore the analysis of electron drift motion does yet properly treat the drift motion of relativistic electrons. A fully relativistic treatment is beyond the scope of this study. We expect that the nonrelativistic treatment is a good first-order approximation to the true drift motion. The predictions of ion motion apply with no limitations because the ions used in this study have nonrelativistic energies.

Finally, we compare our results to results based on a dipole field model. Figure 7 shows projections along the drift shells defined by the TU-82 field model (solid lines) and a dipole field model (dashed lines). Lines for only two energies, 117 and 219 keV are shown, whereas actual predictions were made with all available energies. The two sets of curves naturally begin at the same time and location since this is defined by the times the injection peaks were observed at spacecraft C.

Recalling that the slopes of the lines are determined by drift velocity, we see that the dipole lines are straight, signifying a constant velocity of approximately 72 m/s for 117-keV protons. The drift velocities obtained using the TU-82 model are a function of local time, as we have seen, and range between 64 and 84 m/s for the 117-keV protons shown here. The time of injection predicted using either field model is 4.87 UT. The location of the predicted western boundary is different though. Rather than the -47° predicted using TU-82, the prediction using the dipole field is -37° which is in somewhat worse agreement with the observations from spacecraft A. For electrons the difference between the drift model predictions using the TU-82 field model and a dipole field model are expected to be somewhat larger because of the lower energies involved but again the lack of a fully relativistic calculations prevents us from making a detailed comparison.

CONCLUSIONS

We have presented some of the characteristics of the TU-82 model magnetic field which are of importance to studies of geosynchronous charged particle drifts. We find that the field model is a reasonable representation of the real field under some conditions. Naturally, it also has certain limitations. The model represents an average configuration of the field for various disturbance levels characterized by K_p . Therefore important temporal variations are neglected. More importantly, we feel that neglecting to separate the compression of dayside fields and stretching of nightside fields is inappropriate for drifting particles which are sensitive to the effects of both. We look forward to applying the most recent version of the model [Tsyganenko, 1989] which includes a more continuous transition from ring to tail currents.

Using the TU-82 (or virtually any other) field model, we can solve the equations of motion for bounce average gradient-curvature drift numerically. We have described our drift model in some detail. We have studied the motion of charged particles in the TU-82 field using this drift model which confirmed some expected behaviors and revealed some unexpected ones. There are substantial differences between the bounce average drift velocities and the drift velocities at a single point. This is particularly true when the field is more distorted. We found that drift velocity does not increase monotonically with pitch angle on highly compressed field lines. In stretched tail field lines the drift velocity may actually decrease slightly at local midnight, although this may be an artifact of the particular TU-82 current systems. Drift shell splitting can strongly affect the drift velocities as well as the

location of the drift shells. It is even possible for large pitch angle particles to have longer drift periods than lower pitch angle particles.

We have interpreted the injection which occurred on October 16, 1983 using direct particle injection signatures and model predictions. During this injection the spacecraft carrying the CPA instruments were particularly well positioned to study the event. Spacecraft A and B were located in what we refer to as the injection periphery; locations in which particles of one species show a dispersionless injection, while particles of the other species do not. Observations of energy dispersion in the injection peaks indicate that the bulk of injected particles lie between these two spacecraft. To our knowledge, this is the first report of the existence of an injection periphery region bounding the main injection region. We speculate that the injection periphery is the result of particle drifts which occur as the particles move Earthward from an acceleration region deeper in the magnetotail.

Projections from the remote observation of injected ion and electron pulses predicted an injection region which agreed very well with the observations from spacecraft located near the edges of the injection region. For the event analyzed here the injection region spans about 45° and is west of midnight. Our ability to predict the location of the injection region depends on how well the model field represents the real field. Comparison of measured and model drift periods shows that the TU-82 field is a good representation of the global geosynchronous field for this event. Our ability to predict injection times from remote observations requires only that drift velocities be linearly related to energy. Predictions from all three spacecraft agree to within about 1 min.

Acknowledgements. This work was supported by the Department of Energy and the Geosciences Program of the Office of Basic Energy Science.

The editor thanks K. A. Pfizter and R. J. Walker for their assistance in evaluating this paper.

REFERENCES

- Akasofu, S. I., Physics of Magnetospheric Substorms, D. Reidel, Hingham, MA, D. Reidel, 1977.
- Arnoldy, R. L., and K. W. Chan, Particle substorms observed at the geostationary orbit, *J. Geophys. Res.*, 74, 5019, 1969.
- Baker, D. N., R. D. Belian, P. R. Higbie, and E. W. Hones, High-energy magnetospheric protons and their dependence on geomagnetic and interplanetary conditions, *J. Geophys. Res.*, 84, 7138, 1979.
- Baker, D. N., W. Aiello, J. R. Asbridge, R. D. Belian, P. R. Higbie, R. W. Kebedesel, J. G. Laros, and E. R. Tech, Los Alamos energetic particle sensor systems at geostationary orbit, paper presented at 23rd Aerospace Science Meeting, American Institute of Aeronautics and Astronautics, Reno N.V., Jan. 1985.
- Belian, R. D., D. N. Baker, P. R. Higbie, and E. W. Hones, Jr., High-resolution energetic particle measurements at 6.6 Re, 2: High-energy proton drift echoes, *J. Geophys. Res.*, 83, 4857, 1978.
- Belian, R. D., D. N. Baker, E. W. Hones, P. R. Higbie, S. J. Bame, and J. R. Asbridge, Timing of energetic proton enhancements relative to magnetospheric substorm activity and its implication for substorm theories, *J. Geophys. Res.*, 86, 1415, 1981.
- Bogott, F. H., and F. S. Moser, Drifting energetic particle bunches observed on ATS 5, *J. Geophys. Res.*, 79, 1825, 1974.
- Bogott, F. H., and F. S. Moser, ATS 5 observations of energetic proton injection, *J. Geophys. Res.*, 78, 8113, 1973.
- Brent, R. P., Algorithms for Minimization Without Derivatives, Prentice-Hall, Englewood Cliffs, N.J., 1973.
- Brewer, H. R., M. Schultz, and A. Eviatar, Origin of drift-periodic echoes in outer-zone electron flux, *J. Geophys. Res.*, 74, 159, 1969.
- Chanteur, G., R. Gendrin, and S. Perraut, Experimental study of high-energy electron drift echoes observed on board ATS 5, *J. Geophys. Res.*, 82, 5231, 1977.
- Dahlquist, G., and A. Björck, Numerical Methods, Prentice-Hall, Englewood Cliffs, N.J., 1974.
- DeForest, S. E., and C. E. McIlwain, Plasma clouds in the magnetosphere, *J. Geophys. Res.*, 76, 3587, 1971.
- Fehlberg, E., Klassische Runge-Kutta-formeln vierter und niedrigerer ordnung mit schrittweitenkontrolle und ihre anwendung auf warmeleitungs-probleme, *Computing*, 6, 61, 1970.
- Forsythe, G. E., M. A. Malcolm, and C. B. Moler, Computer Methods for Mathematical Computations, Prentice-Hall, Englewood Cliffs N.J., 1977.
- Higbie, P. R., R. D. Belian, and D. N. Baker, High-resolution energetic particle measurements at 6.6 Re 1: Electron micropulsations, *J. Geophys. Res.*, 83, 4851, 1978.
- Kivelson, M. G., and D. J. Southwood, Approximations for the study of drift boundaries in the magnetosphere, *J. Geophys. Res.*, 80, 3528, 1975.
- Pfizter, K. A., and J. R. Winckler, Intensity correlations and sub-storm electron drift effects in the outer radiation belt measured with the OGO-3 and ATS-1 satellites, *J. Geophys. Res.*, 74, 5005, 1969.
- Mead, G. D., and D. H. Fairfield, A quantitative magnetospheric model derived from spacecraft magnetometer data, *J. Geophys. Res.*, 80, 523, 1975.
- Roederer, J. G., Dynamics of Geomagnetically Trapped Radiation, Springer-Verlag, New York, 1970.
- Reeves, G. D., T. A. Fritz, T. E. Cayton, and R. D. Belian, Multi-satellite measurements of the substorm injection region, *Geophys. Res. Lett.*, 17, 2015, 1990.
- Tsyganenko, N. A., and A. V. Usmanov, Determination of the magnetospheric current system parameters and development of experimental geomagnetic field models based on data from IMP and HEOS satellites, *Planet. Space Sci.*, 30, 985, 1982.
- Tsyganenko, N. A., A Magnetospheric magnetic field model with a warped tail current sheet, *Planet. Space Sci.*, 37, 5, 1989.
- Walker, R. J., K. N. Erickson, and J. R. Winckler, Pitch angle dispersion of drifting energetic protons at synchronous orbit, *J. Geophys. Res.*, 83, 1595, 1978.
- R. D. Belian, T. A. Fritz, and G. D. Reeves Los Alamos National Laboratory, Los Alamos, NM 87545

(Received July 16, 1990;
revised March 26, 1991;
accepted April 3, 1991.)

FIGURE CAPTIONS

Fig. 1. Field line traces in the TU-82 field model. Conditions are for June 21, 1983, 16.67 UT, $Kp=3$. Field lines at noon, dusk, and midnight which lie on a common drift shell are shown in a coordinate system defined by a line from the Earth's center to the magnetic equator for each field line. The effects of dipole tilt, compression on the noon field, and stretching of the tail field can be seen.

Fig. 2. A comparison of field magnitudes from the GOES 6 spacecraft and predictions of the TU-82 field for its least stressed ($Kp=0$) and most stressed ($Kp>3+$) cases.

Fig. 3. TU-82 field lines at midnight for June 21, 1983, 16.67 UT. A hypothetical spacecraft at 6.6 Re on the geographic equator defines the "original field line" for $Kp=0$. For $Kp=3$ the shape of the field line passing through the spacecraft is relatively unchanged while the field line defined by the earth intercept reveals how stretched the original field line becomes.

Fig. 4. A schematic of the drift shell tracing method. The invariants are defined by the field line attached to the satellite for a particular observation. We numerically search for field lines with the same invariants and calculate the bounce average drift velocities (see text).

Fig. 5. (A) The instantaneous gradient, curvature, and gradient-curvature drift velocities for each point along a field line at noon for $Kp=0$ are shown. The instantaneous gradient-curvature drift velocity for $Kp=3$ is also shown. The local minimum near the magnetic equator is the result of reduced curvature drift when the field is compressed. (B) Gradient-curvature drift velocities along field lines at noon, dusk, and midnight. Also shown are the bounce average drift velocities. All field lines are for $Kp=3$ pitch angle = 45° on June 21, 1983, 16.67 UT, and all share the same invariants.

Fig. 6. The bounce average drift velocity as a function of local time for $Kp=0, 2, 3$. The drift shells are defined for June 21, 1983, 16.67 UT for a 45° , 100-keV proton starting at local noon on the geographic equator at 6.6 Re .

Fig. 7. The radial distance to the magnetic equator for the same conditions as Figure 6.

Fig. 8. The radial distance to the magnetic equator for pitch angles of 5° , 30° , 60° , and 85° . Again the drift shells are defined for 6/21/83, 16.67 UT, $Kp=3$ for a 100-keV proton on the noon equator. The effects of drift shell splitting are apparent.

Fig. 9. The bounce average angular drift velocity, $\dot{\phi}$, for the drift shells of Figure 8. At local midnight $\dot{\phi}$ increases for increasing pitch angle. However, because of the compression of the field at noon 30° particles drift faster than 85° particles there.

Fig. 10. The magnetic field strength and invariant integral at hypothetical spacecraft located at different local times. These quantities define a different drift shell at each local time for a 100-keV proton with a pitch angle of 45° and $Kp=3$. The overall field is defined for a single universal time of 16.67 UT on June 21, 1983.

Fig. 11. The invariant integral and magnetic field magnitude for a 45° , 100-keV proton for $Kp=3$. Unlike figure 10 we fix the position of a hypothetical satellite at local noon and let the Terrestrial field rotate through 24 hours of universal time. The x axis is defined by the direction toward which the magnetic axis points.

Fig. 12. The locations of the three spacecraft and their drift shell. The drift shells are a projection of the magnetic equators into the X - Y GSE plane. Spacecraft B and C share nearly the same drift shell, while spacecraft A lies at slightly higher L . Also shown, schematically, is the injection region which is defined by observations from spacecraft A and B.

Fig. 13. Observations from spacecraft A and B. The top panels show two electron energy ranges and the bottom panels show two ion energy ranges. These observations show that spacecraft A is in the 'ion periphery' region to the west of the injection region and that spacecraft B is in the 'electron periphery' to the east (see text).

Fig. 14. The correlation of model and measured drift periods. Measured drift periods are derived from electron drift echoes using spin-averaged data. Model drift periods are shown for the TU-82 model for 45° electrons under conditions of $Kp=0$ (circles and long dashes) and $Kp=3$ (squares and short dashes). The solid line represents perfect agreement. The $Kp=0$ condition gives somewhat better agreement as would be expected if the field is relaxed after substorm injection.

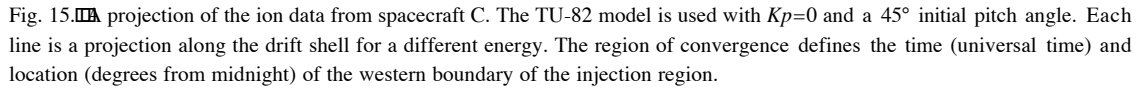
Fig. 15.  projection of the ion data from spacecraft C. The TU-82 model is used with $Kp=0$ and a 45° initial pitch angle. Each line is a projection along the drift shell for a different energy. The region of convergence defines the time (universal time) and location (degrees from midnight) of the western boundary of the injection region.

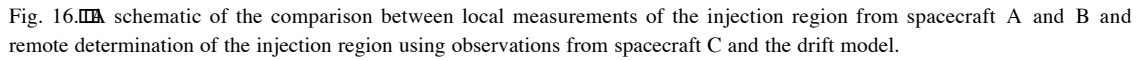
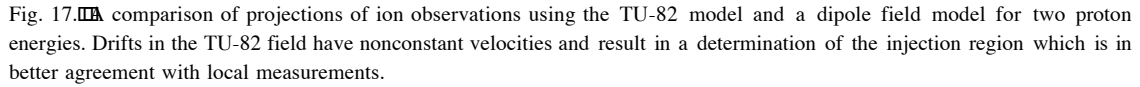
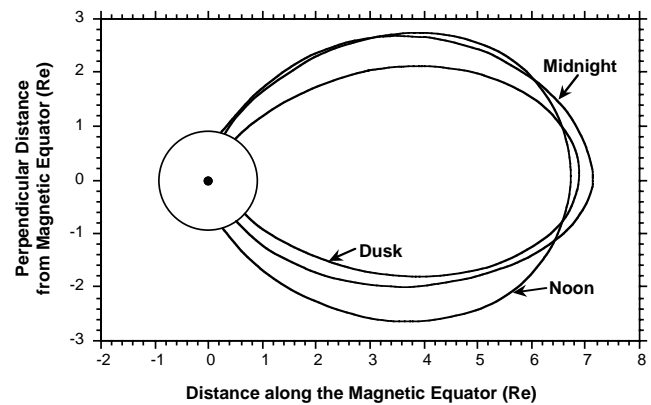
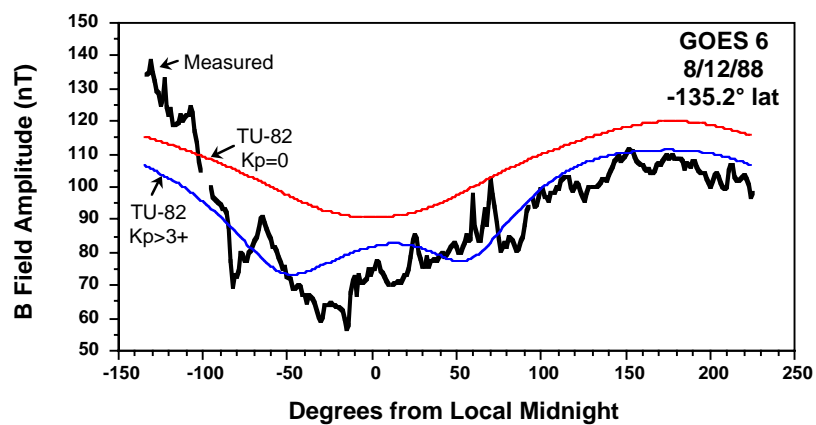
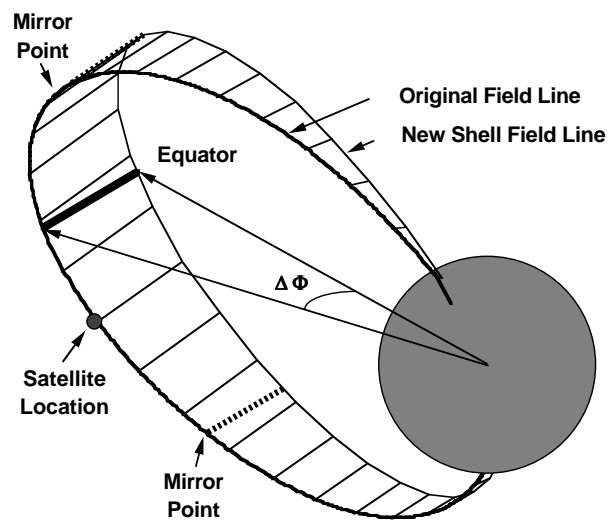
Fig. 16.  schematic of the comparison between local measurements of the injection region from spacecraft A and B and remote determination of the injection region using observations from spacecraft C and the drift model.

Fig. 17.  comparison of projections of ion observations using the TU-82 model and a dipole field model for two proton energies. Drifts in the TU-82 field have nonconstant velocities and result in a determination of the injection region which is in better agreement with local measurements.







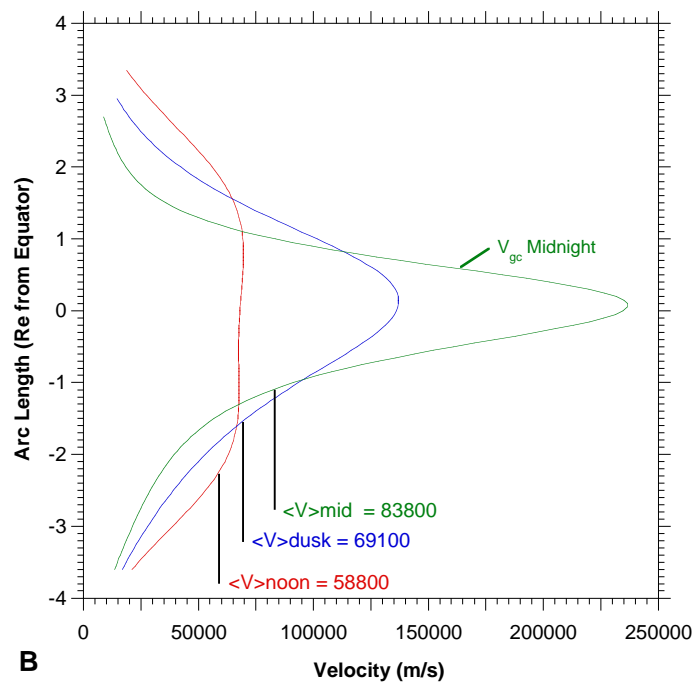
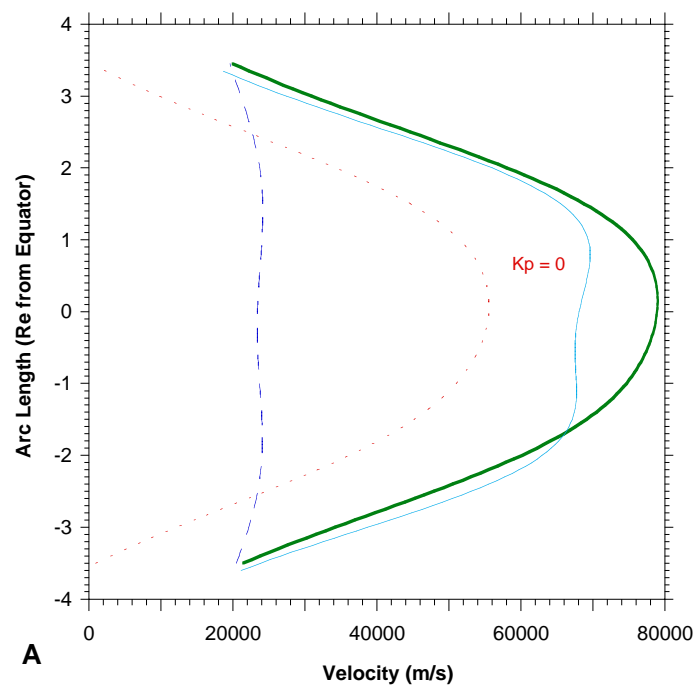
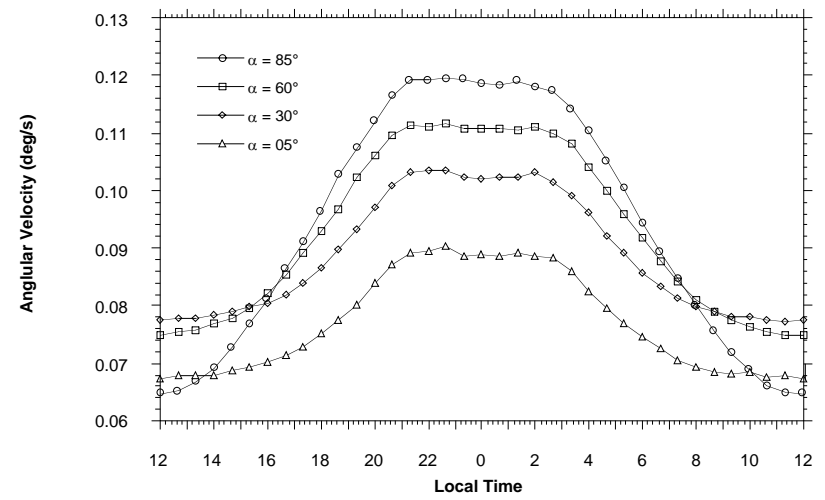
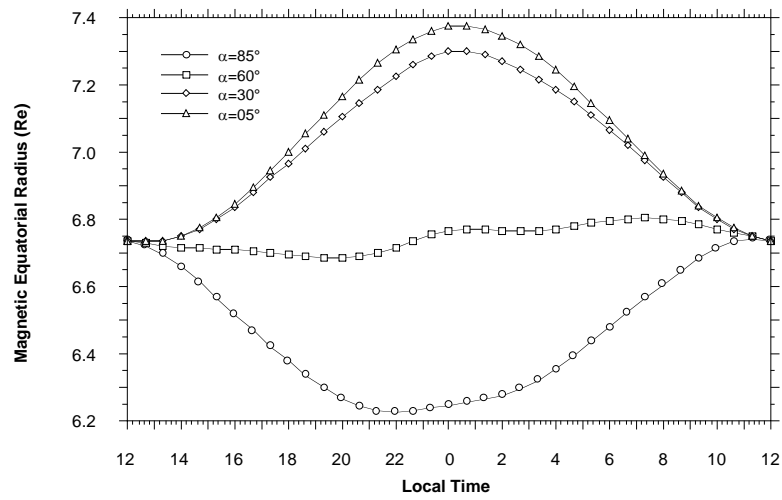
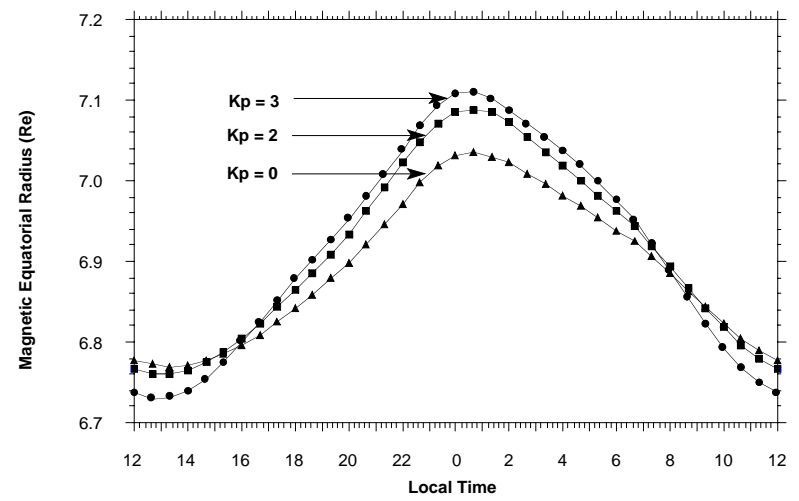
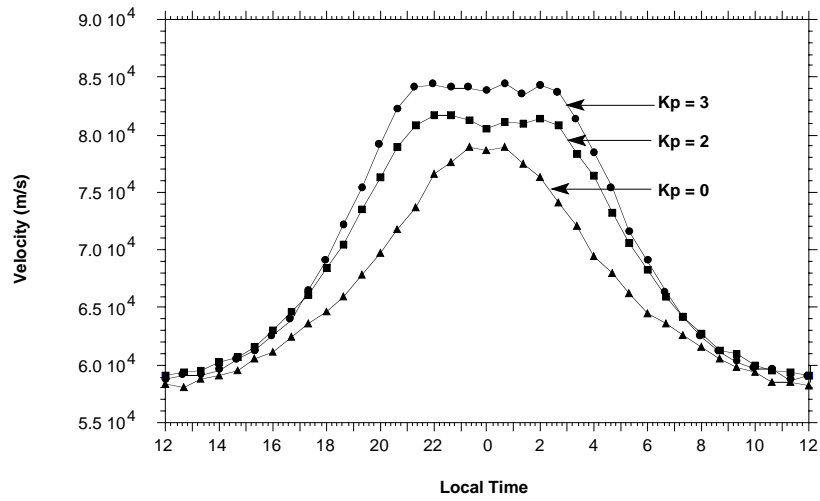
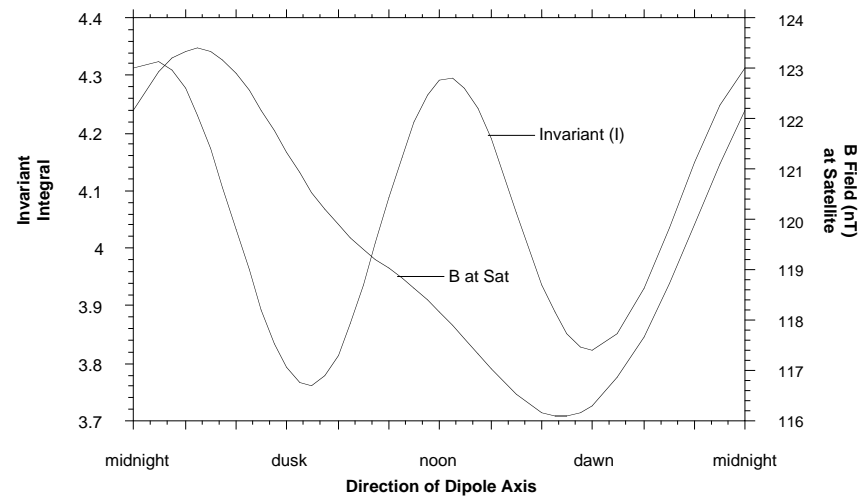
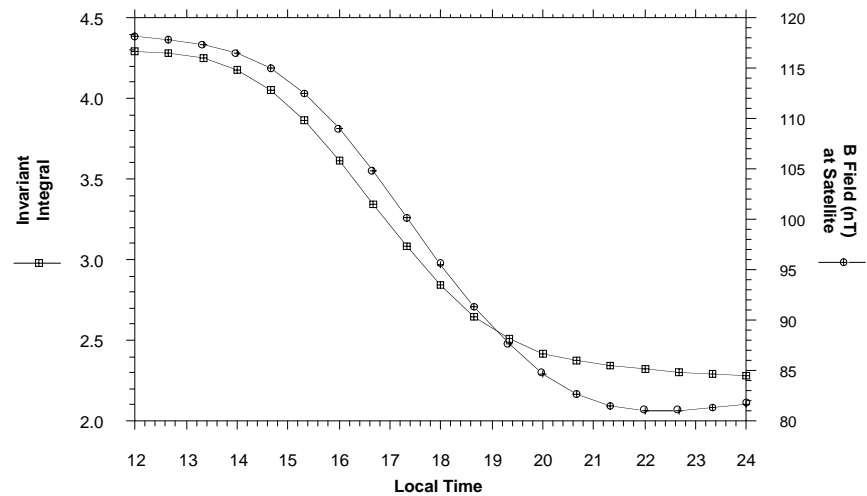
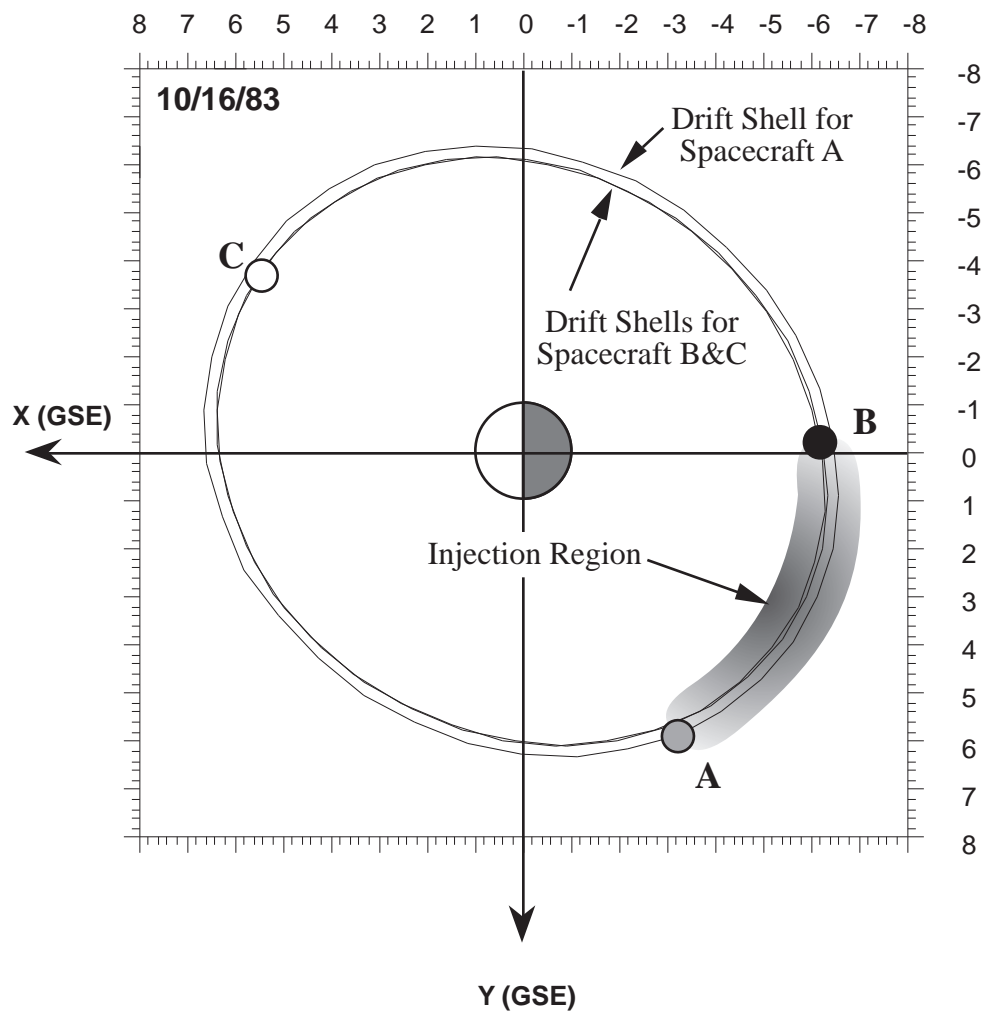


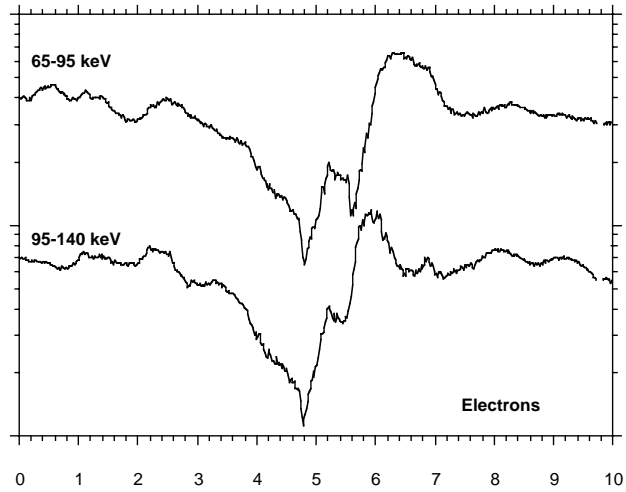
Figure 5



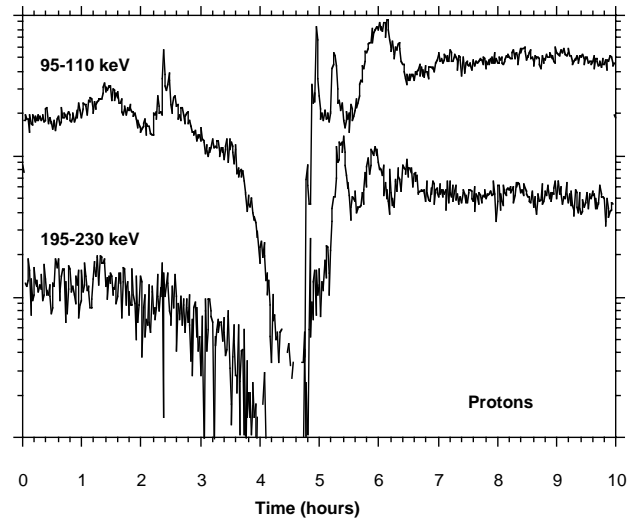
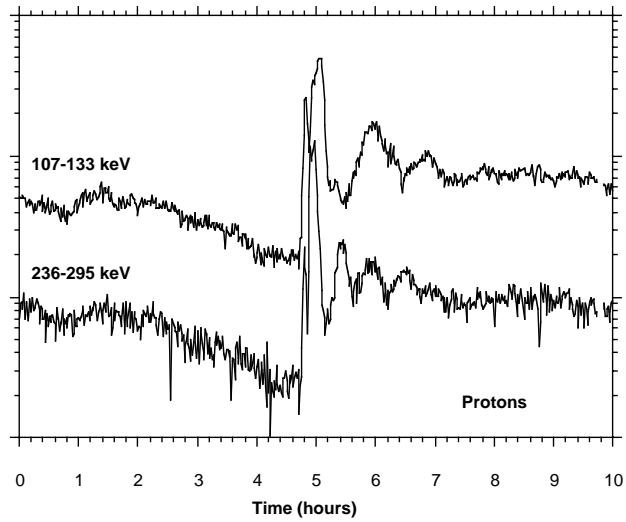
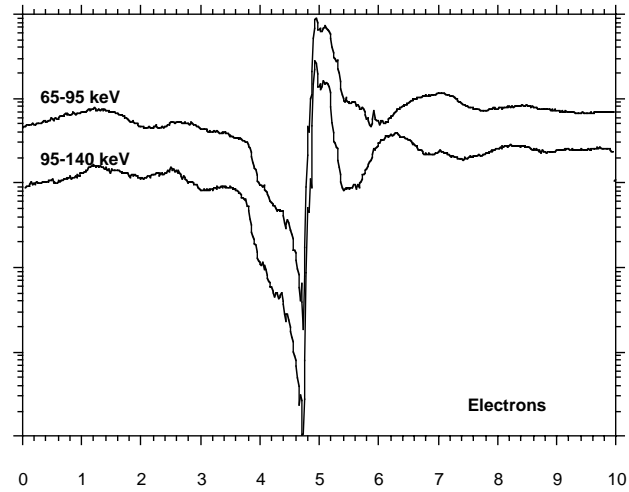


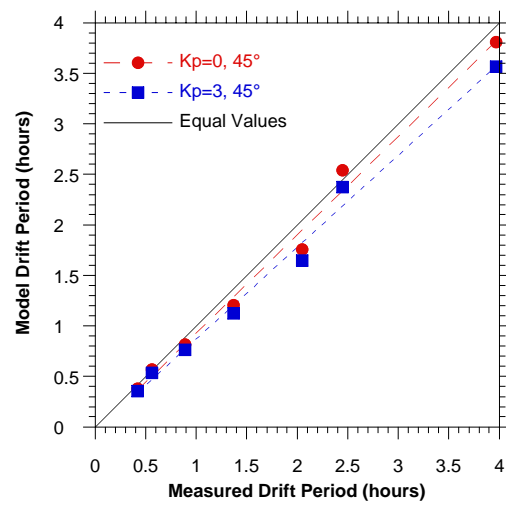


Spacecraft A
20.0 LT

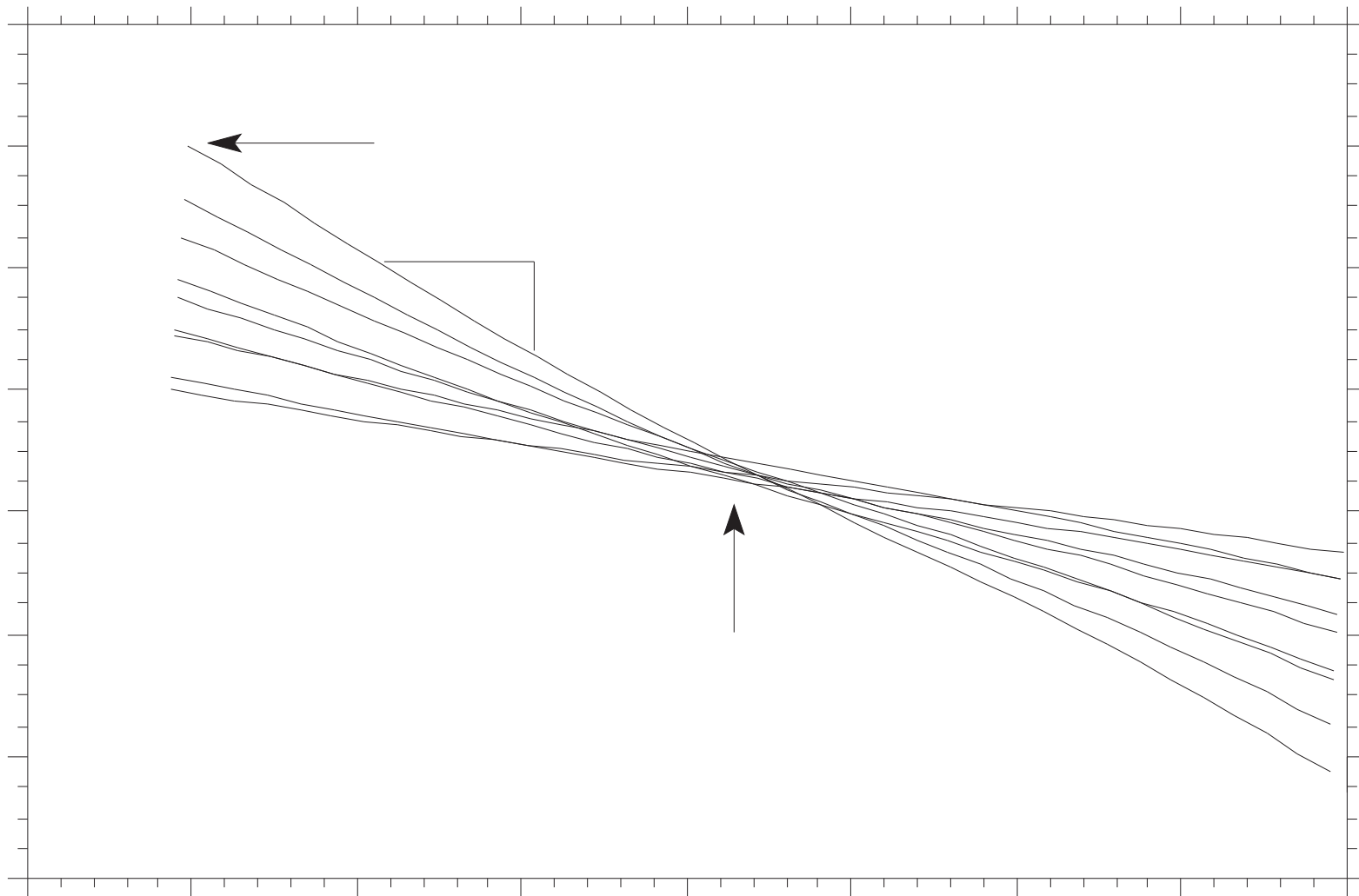


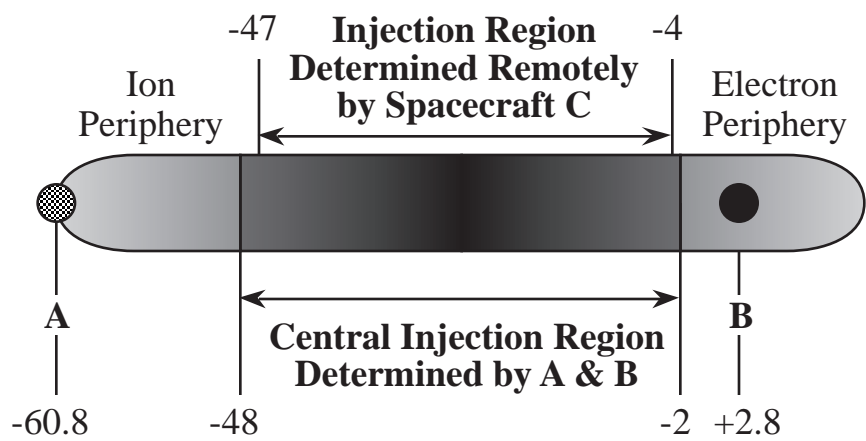
Spacecraft B
00.3 LT





Universal Time (hours)





Comparison of Dipole and TU-82 for Spacecraft C Ion Peaks

